Line shapes of cascade two-photon transitions in a cesium magneto-optic trap

J. H. Marquardt, H. G. Robinson, and L. Hollberg

National Institute of Standards and Technology, Boulder, Colorado 80303

Received August 16, 1995; revised manuscript received November 30, 1995

We present a study of a two-photon double-resonance transition in cold cesium atoms in a magneto-optic trap. A closed five-level density matrix model of the system is developed to characterize the double-resonance Autler–Townes-split absorption line shape. Comparing this model with experimental spectra, we gain insight into the dominant process involved in trapping atoms, in particular, the importance of the interference of the six trapping laser beams. This system is used to probe transient effects in the trap as well as collective effects of the trapped atom cloud resulting from the intentional misalignment of the trapping beams.

1. INTRODUCTION

We investigate the detailed line shapes of cascade two-photon transitions in laser-cooled and trapped atoms. There has been much research on the use of cold, trapped atoms for microwave frequency standards,[1] ultracold atom collisions,[2] and spectroscopic dynamics of cold, trapped atoms.[3] Some of this research has lead to surprising results in terms of narrow optical resonances, evidence of quantized motion, atomic localization in atom traps,[4] and other effects. Various mechanisms that produce low temperatures in these traps are now understood. In addition, some theoretical models are now able to calculate detailed line shapes of the spectroscopic features observed on the cooling and trapping transitions.[5] Other effects, including some aspects of the collective behavior of trapped atoms and unusually long relaxation times remain unexplained. Further detailed spectroscopic investigations of cold, trapped atoms promise new surprises as we learn more about their environment.

Our experiment consists of optically probing cold, trapped cesium atoms, which are excited to the $6P_{3/2}$ state by the absorption of the cooling and trapping laser. A probe laser, tuned to the $6P_{3/2} \rightarrow 9S_{1/2}$ transition at 658.8 nm, is sent through the trapped atoms, creating a doubly resonant two-photon transition (Fig. 1). The probe field is weak and nonperturbing and completely independent of the trapping laser fields. In our experimental work we observed relatively narrow Rabi-split two-photon line shapes that are reminiscent of atomic beam studies of Gray and Stroud and of Hemmer *et al.*,[6] except that in our case the atoms are cooled and trapped by the resonant radiation and a weak magnetic field. The system consists of magnetic-field gradients and strong laser fields at 852 nm necessary for the trapping of the atoms in the usual $\sigma^+ - \sigma^-$ magneto-optic trap (MOT) configuration. The signal that we observe is the absorption of the 658.8-nm laser as it is tuned across the two-photon resonance. Because the splitting and the shape of the absorption signal depend on the properties of the trap, understanding the features of the line shape provides knowledge of the local environment of the atoms. Independently probing the perturbing effects of the trapping fields will be important in future realizations of optical frequency and length standards based on laser-cooled and trapped atoms.

Initially, we developed a simple theoretical model describing this double-resonance experiment,[7] which showed the qualitative features of the experimental line shape but quantitatively was not in good agreement with the experimental results. We have improved the model by including important additional effects, such as the three-dimensional nature of laser field and intensity distributions and the effects of laser beam phase fluctuation. In this paper we present a detailed description of this improved model and its comparison with the experimental data.

2. EXPERIMENT

The cesium atoms are cooled and trapped in a standard vapor-cell MOT. Our MOT is similar to those described in the literature[8] and is shown schematically in our experimental setup in Fig. 2. We use two extended-cavity diode lasers for the trap, one relatively powerful laser (~30 mW) for cooling and trapping and a second laser (~1 mW) to recirculate atoms that have fallen into the $F = 3$ hyperfine ground state. The cooling and trapping light is tuned to the low-frequency side of the $6S_{1/2}$, $F = 4 \rightarrow 6P_{3/2}$, $F = 5$ cycling transition. To lock the trapping laser at a specific detuning, the laser beam is sent through an acousto-optic modulator (AOM), where a small percentage of the light is frequency shifted and sent through a separate cesium cell used for saturated absorption. The laser is locked to the saturated-absorption signal corresponding to the nearest crossover resonance to the $6S_{1/2}, F = 4 \rightarrow 6P_{3/2}, F = 5$ transition. The frequency of the trapping laser is controlled by use of a rf synthesizer to drive the AOM. The repumping laser is tuned to the $6S_{1/2}, F = 3 \rightarrow 6P_{3/2}, F = 3$ or $F = 4$ transition and locked to the side of the cesium Doppler profile in a second, separate cesium cell. The $6P_{3/2}$ state of the trapped atoms is then interrogated by direct absorption of a diode laser tuned to the excited $6P_{3/2}$, $F = 5 \rightarrow 9S_{1/2}$, $F = 4$ transition at 658.8 nm. Approximately 1.5 mW of 658.8-nm light was provided by an extended-cavity diode laser.

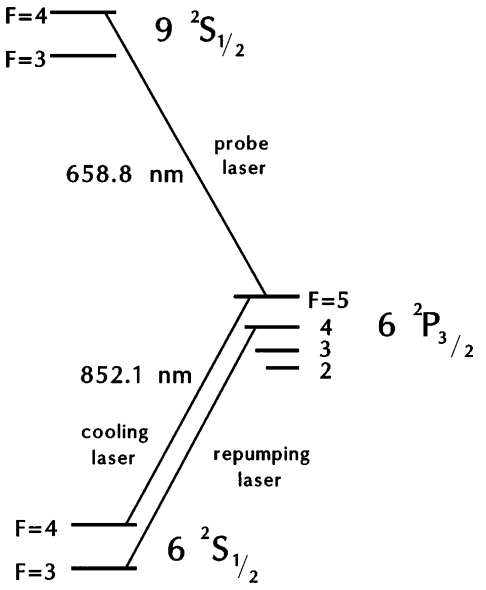

Fig. 1. Relevant cesium energy levels and the hyperfine structure, showing the lasers used for the magneto-optic trap and the cascade two-photon transition.

This laser was frequency stabilized to a reference cavity, which resulted in a short-term linewidth of ~500 Hz with low-frequency jitter of ~5 kHz. The laser's spatial mode was filtered by an optical fiber, which delivered the light to the experiment. The probe laser was elliptically polarized and copropagated with one of the six trapping beams. The diameter of the probe beam was set approximately equal to the diameter of the trapped atom cloud. After spatial filtering, frequency stabilization, and amplitude noise subtraction, the probe laser power available at the MOT was ~40 μW. The absorption on the 658.8-nm transition by the cesium-atom cloud (~10^8 cold atoms) was typically ~1%. (Fluorescence detection could have been chosen as well but would have required good imaging optics, filtering of the strong 852-nm light, etc. Absorption detection was chosen because of its relative simplicity.) The power of the probe beam was low enough that it did not appear to perturb the trap dynamics or the profile of the absorption line shape.

A typical absorption spectrum of the 658.8-nm probe laser is shown in Fig. 3. The doubly peaked profile of this transition is attributed to the optical Autler–Townes effect (ac-Stark splitting). Because of the strong trapping laser fields, we expect a doublet structure of the coupled ground and the first excited states. These states exhibit a well-defined generalized Rabi splitting that depends on the detuning and the Rabi frequency of the trapping laser and the decay rates of the atomic states (the Rabi frequency is given by $\alpha_{21} = \mu_{21}E_{21}/\hbar$, where μ_{21} is the dipole matrix element and E_{21} is the amplitude of the laser field driving the $6S_{1/2} \rightarrow 6P_{3/2}$ transition).

The characteristics of the line shape were investigated as functions of various trap parameters. For example, Fig. 4 shows the variation of individual 658.8-nm absorption line shapes with detuning of the trapping laser frequency. In this figure the centers of the larger peak were aligned (in frequency space) to show clearly the dependence of the splitting on the trap detuning. We can compare these individual line shapes with theory to evaluate our model of the trapping environment. In particular, we studied the Autler–Townes splitting, the peak height ratios, and the widths of the absorption peaks as a function of the trap parameters. This gave valuable information about the local fields in the trap. The detuning of the trapping laser was limited by the range of stable trap operation. The overall height of the signal in the figure varied with the number of trapped atoms, obviously a function of the detuning. The maximum signal corresponded to a magnetic field gradient of $\sim 15 \times 10^{-4}$ T/cm (~15 G/cm) and a detuning of ~2Γ to the low-frequency side of the transition ($\Gamma/2\pi = 5.1$ MHz is the natural linewidth for this transition in cesium).

3. THEORY

We have developed a theoretical model of the two-photon transition that includes many of the physical processes that affect the atomic spectra of the trapped atoms. It

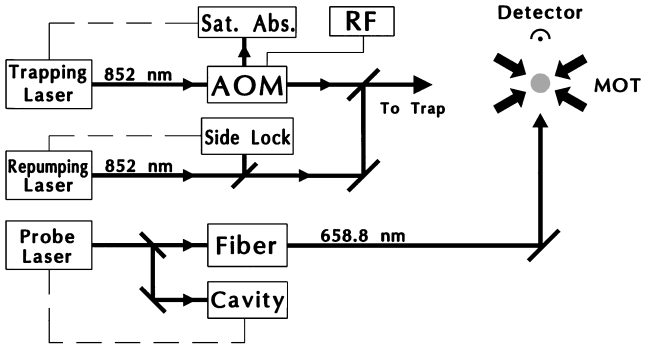

Fig. 2. Schematic diagram of the experimental laser setup. The trapping laser is locked to a saturated-absorption crossover feature in a separate cesium cell. The AOM is used to frequency offset the lock point from the saturated-absorption (Sat. Abs.) feature. The repumping laser is locked to the side of the Doppler profile in a different cesium cell. The dashed lines represent servo loops needed to lock the lasers. The vertical pair of trapping beams and the magnetic-field coils are not shown. The detectors are used to monitor direct absorption of the probe beam and trap fluorescence.

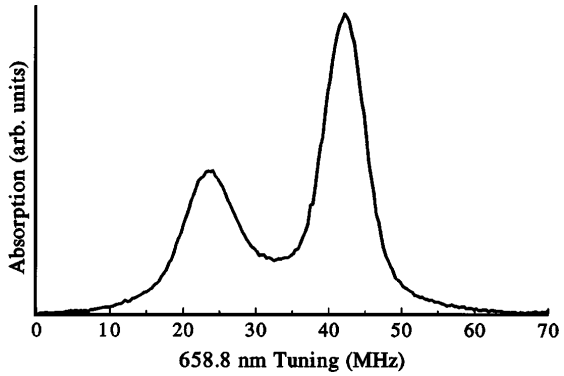

Fig. 3. Typical absorption spectrum taken in our MOT with standard σ^+/σ^- laser polarizations. The trap detuning ($\delta_{21}/2\pi$) was 10 MHz; $\partial \mathbf{B}_{\text{trap}}/\partial z = 16 \times 10^{-4}$ T/cm (16 G/cm). Cloud diameter ~3.5 mm, ~2.5 mm in height, ~10^8 atoms, effective Rabi frequency α_{21} of 15.5 MHz. The 658.8-nm laser is swept through the resonance with the trapping lasers kept fixed. The x axis shows the relative tuning of the 658.8-nm laser. The selection of the origin is arbitrary. To improve the signal-to-noise ratio this spectrum is averaged over 20 scans.

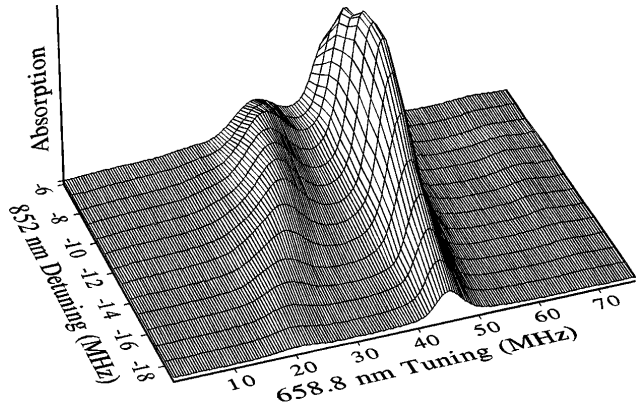

Fig. 4. Probe absorption as a function of trapping laser detuning, $\delta_{21}/2\pi$. The large peaks were aligned to show clearly the dependence of the cascade two-photon line shape on the trap laser detuning. The signal height depends on the number of atoms in the trap, a function of the detuning. The small features at ~20 and ~70 MHz are sidebands put on the 658.8-nm laser as a frequency reference. These spectra were averaged over 200 scans to improve the signal-to-noise ratio. The figure is adapted from Ref. 7.

would be extremely difficult to analyze the complete system theoretically, including all relevant atomic levels in cesium, six strong laser fields, laser polarizations, the three-dimensional variation of the magnetic field $\mathbf{B}_{\text{trap}}$, and the distribution and the residual motion of the cold atoms in the trap. To analyze a more tractable system we have made some assumptions and simplifications. We have assumed (to a good approximation) that the laser fields are plane waves, the atoms are motionless, and the collisional effects are negligible. We include spatial effects for the three-dimensional trapping laser fields and the variation of $\mathbf{B}_{\text{trap}}$ over the trapping volume. The Zeeman structure for each radiatively coupled level is approximated by use of only the $m_F = \pm F$ (stretched state) Zeeman coefficient for each of the three coupled levels. The validity of our assumptions and simplifications is discussed later in this paper. We have further simplified the complicated cesium energy-level spectra to a closed five-level system (Fig. 5). Three of these levels, $|1\rangle$, $|2\rangle$, and $|3\rangle$, correspond to the three coupled levels of the doubly resonant, cascade configurations $6S_{1/2}, F = 4 \rightarrow 6P_{3/2}, F = 5 \rightarrow 9S_{1/2}, F = 4$. The remaining two levels, $|4\rangle$ and $|5\rangle$, are artificial and represent all other decay channels out of the cascade system, which are due to the other atomic states and to the relevant hyperfine structure of the three coupled levels. The hyperfine structure permits population decay out of the $6S_{1/2}, F = 4 \rightarrow 6P_{3/2}, F = 5$ cycling transition by off-resonant absorption and decay to the $6S_{1/2}, F = 3$ ground state. This loss mechanism and the presence of the repumping laser are represented in our model by the addition of level $|5\rangle$. The rate at which atoms enter the other hyperfine states can be calculated and is represented in the model by γ_{25}. Similarly, we have added level $|4\rangle$ to represent other decay channels out of the excited, $9S_{1/2}, F = 4$, state to the other noncoupled states. This rate is represented by γ_{34} and shown in Fig. 5. Following the standard approach, we model our system by using the density matrix formalism.[9] Some additions and modifications to this approach are necessary for the conditions relevant to this experiment.

The time evolution of the density operator can be represented by

$$\frac{d\rho_{nn}}{dt} = -\frac{i}{\hbar}[\hat{H}, \hat{\rho}]_{nn} + \sum_k \{\gamma_{kn}\rho_{kk} - \gamma_{nk}\rho_{nn}\} \qquad \text{for } n = m,$$

$$\frac{d\rho_{nm}}{dt} = -\frac{i}{\hbar}[\hat{H}, \hat{\rho}]_{nm} - \Gamma_{nm}\rho_{nm} \qquad \text{for } n \neq m. \tag{1}$$

Here the $\hat{H}$ is the Hamiltonian operator of the system and γ_{nm} is the decay rate from state n to state m. (In this representation $\gamma_{nm} \neq \gamma_{mn}$. If state n is a higher-energy state than state m, then $\gamma_{mn} = 0$.) The damping rate Γ_{nm} of the off-diagonal elements can be written as

$$\Gamma_{nm} = \frac{1}{2}(\gamma_n + \gamma_m) + \gamma_{nm}^{\text{col}}, \tag{2}$$

where γ_n and γ_m represent the total decay rates out of levels n and m and γ_{nm}^{col} is the dipole dephasing term that is due to processes such as collisions (which we neglect).

We can write the Hamiltonian operator as

$$\hat{H} = \hat{H}_0 + \hat{V}(t), \tag{3}$$

where $\hat{H}_0$ is the atomic Hamiltonian and $\hat{V}(t)$ represents the interaction energy of the atom with the electromagnetic field. $\hat{V}(t)$ can be represented by

$$V_{nm}(t) = \mathcal{E}_{nm} \cos \Omega_{nm} t = \frac{-\boldsymbol{\mu}_{nm} \cdot \mathbf{E}_{nm}}{2}[\exp(-i\Omega_{nm}t) + \exp(i\Omega_{nm}t)], \tag{4}$$

where $\mathbf{E}_{nm}$ is the incident laser field with frequency Ω_{nm} and $\boldsymbol{\mu}_{nm}$ is the dipole matrix element corresponding to the transition from level m to level n. The rotating-wave approximation allows us to neglect the last term in Eq. (4). After inserting the full Hamiltonian $\hat{H}$ into Eqs. (1), we can write

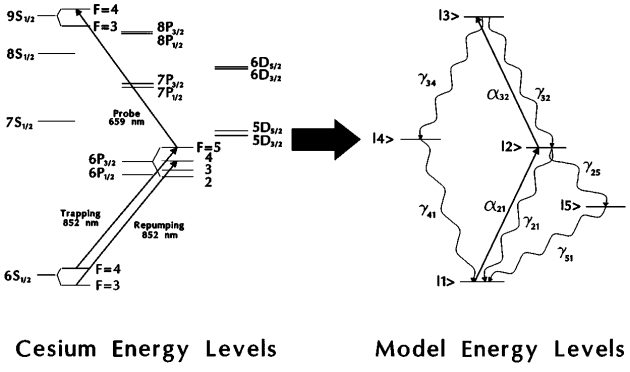

Fig. 5. Relevant cesium energy-level diagram showing the cascade two-photon transition, the lasers used in the experiment, and the corresponding energy levels of the model. The energy levels of the model consist of three levels that are coupled by laser radiation, $|1\rangle$, $|2\rangle$, and $|3\rangle$, and two artificial levels, $|4\rangle$ and $|5\rangle$, representing all the other decay channels out of the cascade system. The γ are the decay rates between levels, and the α are the Rabi frequencies of the lasers used in the model.

$$\left(\frac{\partial}{\partial t} + i\omega_{nm}\right)\rho_{nm} + \frac{i}{\hbar}\sum_k (V_{nk}\rho_{km} - \rho_{nk}V_{km}) = \begin{cases} \sum_k (\gamma_{kn}\rho_{kk} - \gamma_{nk}\rho_{nn}) & \text{for } n = m \\ -\Gamma_{nm}\rho_{nm} & \text{for } n \neq m \end{cases}, \quad (5)$$

where $\omega_{nm} = E_n - E_m/\hbar$ is the transition frequency between levels n and m. Introducing the slowly varying quantity σ_{nm}, such that

$$\rho_{nm}(t) = \sigma_{nm}(t)\exp(-i\Omega_{nm}t), \quad (6)$$

we look for steady-state ($d\sigma_{nm}/dt = 0$) solutions to Eq. (5); these yield

$$\sum_k (\gamma_{kn}\sigma_{kk} - \gamma_{nk}\sigma_{nn}) + \frac{i}{2}\sum_k (\alpha_{nk}\sigma_{kn} - \sigma_{nk}\alpha_{kn}) = 0 \quad \text{for } n = m,$$

$$[i(\Omega_{nm} - \omega_{nm}) - \Gamma_{nm}]\sigma_{nm} + \frac{i}{2}\sum_k (\alpha_{nk}\sigma_{km} - \sigma_{nk}\alpha_{km}) = 0 \quad \text{for } n \neq m, \quad (7)$$

where $\Omega_{nm} = -\Omega_{mn}$ and $\alpha_{nm} = -\mathcal{E}_{nm}/\hbar$ in this notation. Equations (7) describe a 25×25 matrix for our five-level system. Fortunately, many of the levels are not coupled by radiation or decay, so some simplifications can be made. In the steady state many of the density matrix states can be written in terms of other states. For example σ_{44} can be eliminated by use of the relation for $d\sigma_{44}/dt$:

$$\frac{d\sigma_{44}}{dt} = \gamma_{41}\sigma_{44} - \gamma_{34}\sigma_{33} = 0 \rightarrow \sigma_{44} = \frac{\gamma_{34}}{\gamma_{41}}\sigma_{33}. \quad (8)$$

Similarly, the other states that are not coupled by laser radiation can be represented in terms of coupled states. This simplifies the 25×25 matrix into a 9×9 matrix (shown in Table 1), which can be solved for each of the remaining density matrix components. In the table $\delta_{nm} = \Omega_{nm} - \omega_{nm}$ represents the detuning of the lasers from exact resonance for the given transition ($\delta_{21} < 0$ for trap operation). The signal is then calculated as a function of the probe laser detuning δ_{32}. Solving this 9×9 density matrix gives the specific values of σ_{nm}. The signal that we observe experimentally is the absorption from level $|2\rangle$ to level $|3\rangle$, which is dependent on the imaginary part of σ_{32}.

4. NUMERICAL IMPLEMENTATION OF THE THEORY

This solution for the imaginary part of σ_{32} gives only part of the total line shape because the three-dimensional nature of the trapping laser and the magnetic fields of the MOT have not yet been included. Because the diameter of the probe beam is set approximately equal to the size of the cloud of trapped atoms, every atom in the trap can contribute to the absorption line shape. The energy levels of the atoms in the trap are position dependent because of both the magnetic-field gradient and the wavelength scale variations of the electric field and polarization. The magnetic-field gradient $\partial\mathbf{B}_{\text{trap}}/\partial\mathbf{r}$ effectively alters the detuning of the trapping laser δ_{21} as a function of the distance from the center of the trap (where $|\mathbf{B}_{\text{trap}}| = 0$). Thus, for a fixed trap detuning, the actual detuning of the trapping laser depends on atomic Zeeman structure as

$$\delta_{21}' = \delta_{21} + \frac{\mu_B}{h}\mathbf{B}_{\text{trap}}(\rho, z)(g_{F'=5}m_{F'} - g_{F=4}m_F). \quad (9)$$

Here $\mathbf{B}_{\text{trap}}(\rho, z)$ is the local magnetic field at point (ρ, z), $g_{F'=5} = 0.4$ and $g_{F=4} = 0.25$ are the Landé g factors, μ_B is the Bohr magneton, and $m_{F'}$ and m_F are the Zeeman sublevels of the excited state and the ground state, respectively. For the anti-Helmholtz configuration the magnetic-field strength $|\mathbf{B}_{\text{trap}}|$ varies approximately linearly with distance from the center of the trap. The atoms at the center of the trap have a detuning that corresponds to the trapping laser detuning, $\delta_{21}'(\rho = 0) = \delta_{21}$, whereas other atoms experience a different detuning, depending on the magnetic-field gradient and the position of the atom. We call the most probable value of δ_{21}' the effective detuning. Larger magnetic fields correspond to smaller effective detunings (for $\delta_{21} < 0$), which naturally affect the cascade two-photon line shape. Of course, it is possible to switch off the magnetic field to eliminate the magnetic-field-dependent effects, but we dedicate most of this discussion to the steady state, which includes the magnetic field.

Unlike that of the magnetic field of the trap, which varies over macroscopic dimensions, the electric field's magnitude changes on a scale smaller than the optical wavelength. The interference of the laser fields in the trap is generated by the intersection of the six circularly polarized laser beams. This interference pattern depends on the relative amplitudes and phases of the six beams and varies significantly, both in magnitude and in polarization, over an optical wavelength. In our model

Table 1. Density Matrix

	σ_{33}	σ_{32}	σ_{31}	σ_{21}	σ_{11}	σ_{12}	σ_{13}	σ_{23}	σ_{22}
σ_{33}	$-\gamma_{34} - \gamma_{32}$	$-i\alpha_{23}/2$	0	0	0	0	0	$i\alpha_{32}/2$	0
σ_{32}	$-i\alpha_{32}/2$	$i\delta_{32} - \Gamma_{32}$	$-i\alpha_{12}/2$	0	0	0	0	0	$i\alpha_{32}/2$
σ_{31}	0	$-i\alpha_{21}/2$	$i(\delta_{32} + \delta_{21}) - \Gamma_{31}$	$i\alpha_{32}/2$	0	0	0	0	0
σ_{21}	0	0	$i\alpha_{23}/2$	$i\delta_{21} - \Gamma_{21}$	$i\alpha_{21}/2$	0	0	0	$-i\alpha_{21}/2$
σ_{11}	γ_{34}	0	0	$i\alpha_{12}/2$	0	$-i\alpha_{21}/2$	0	0	$\gamma_{21} + \gamma_{25}$
σ_{12}	0	0	0	0	$-i\alpha_{12}/2$	$-i\delta_{21} - \Gamma_{21}$	$-i\alpha_{32}/2$	0	$i\alpha_{12}/2$
σ_{13}	0	0	0	0	0	$-i\alpha_{23}/2$	$-i(\delta_{32} + \delta_{21}) - \Gamma_{31}$	$i\alpha_{12}/2$	0
σ_{23}	$i\alpha_{23}/2$	0	0	0	0	0	$i\alpha_{21}/2$	$-i\delta_{32} - \Gamma_{32}$	$-i\alpha_{23}/2$
σ_{22}	γ_{32}	$i\alpha_{32}/2$	0	$-i\alpha_{21}/2$	0	$i\alpha_{12}/2$	0	$-i\alpha_{32}/2$	$-\gamma_{21} - \gamma_{25}$

we neglect any polarization dependencies that would contribute to optical pumping of the atoms to other Zeeman states. A more exact model that includes all the magnetic sublevels and polarization dependencies of the transitions was not attempted because of its complexity. We can write the σ^+ and σ^- beams as

$$\mathcal{E}_{\sigma^+}(z) = E_0[\hat{i}\cos(kz - \omega t + \phi_1) - \hat{j}\sin(kz - \omega t + \phi_1)],$$
$$\mathcal{E}_{\sigma^-}(z) = E_0[\hat{i}\cos(kz - \omega t + \phi_2) + \hat{j}\sin(kz - \omega t + \phi_2)], \tag{10}$$

for waves traveling along the positive z axis. The total field is given by the vector sum of the six intersecting beams with the proper polarization and direction. Initially, choosing all the phases to be 0 ($\phi_n = 0$) allows us to write the total field for our MOT as

$$\mathcal{E}_{tot} = 2E_0\cos\omega t[\hat{i}(\cos kz + \sin ky) + \hat{j}(\cos kx - \sin kz) + \hat{k}(\cos ky + \sin kx)]. \tag{11}$$

We are interested in the time-averaged magnitude of this three-dimensional field, which can be written as

$$|\mathbf{E}_{\text{laser}}| = \sqrt{\mathcal{E}_{tot}\cdot\mathcal{E}_{tot}^*} = E_0[6 + 4(\cos kz\sin ky - \cos kx\sin kz + \cos ky\sin kx)]^{1/2}. \tag{12}$$

Figure 6(a) shows Eq. (12) plotted as a function of x and y with a fixed value for z ($kz = 3\pi/4$). The actual interference pattern depends on the relative phase of each of the six trapping beams and can easily be included in Eq. (12). In the experiment the relative phase of each of the laser beams is unknown and is continually changing owing to mechanical vibrations. These vibrations are important because of the finite sweep speed of the probe laser (generally <200 Hz) and must be taken into account.

Using the laser field distribution above, we generated a Monte Carlo histogram of the probability of finding a specific laser field $|\mathbf{E}_{\text{laser}}|$ in the trap. An initial histogram was calculated with a specific phase distribution ($\phi_n = 0$). To approximate phase-changing mechanical vibrations, we calculated separate histograms for many different phase distributions. These were combined and normalized to form a composite distribution representative of the electric fields in the trap. This composite distribution is shown in Fig. 6(b). With this distribution we can integrate over the fields with the proper weighting of the Rabi frequencies to give the final line shape.

Because of the spatial dependence of the trap's magnetic and electric fields, we need to include all the fields in the spatial distribution to calculate the measured two-photon line shape. We accomplish this by numerically integrating over the magnetic-field contributions while simultaneously integrating over the microscopic interference pattern of the electric field. The total line shape can be represented as a sum of many individual line shapes, each of which corresponds to atoms in different electric and magnetic fields. These line shapes are additionally weighted to ensure that each individual line-shape contribution reflects the number of atoms present in similar fields. We assume that the distribution of atoms is proportional to the intensity of the local electric field.[10] By stepping through the possible values of the electric and the magnetic fields and calculating a separate line shape for each value, we combine these line shapes with the proper weighting to create a final line shape. This absorption line shape S can be represented by

$$S \propto \iiint \mathrm{Im}[\sigma_{32}]P(E)I\rho\,\mathrm{d}E\,\mathrm{d}\rho\,\mathrm{d}z, \tag{13}$$

where $P(E)$ is the probability of finding a certain electric field E in the trap [from Fig. 6(b)], I is the intensity of the radiation, and ρ and z are the radial and the axial positions, respectively, in the trap.[11] We numerically integrate relation (13) over all electric and magnetic fields (all positions in the trap). This procedure produces a line shape that we can compare with experiment. This position-dependent integration ($\mathbf{E}_{\text{laser}}$, ϕ, $\mathbf{B}_{\text{trap}}$) broadens the Rabi-split line shape but does not wash it out. Although each group of atoms in the trap corresponds to a different Rabi splitting, the composite line shape has a single, well-defined value for the splitting. This single Rabi splitting represents the weighted average of the in-

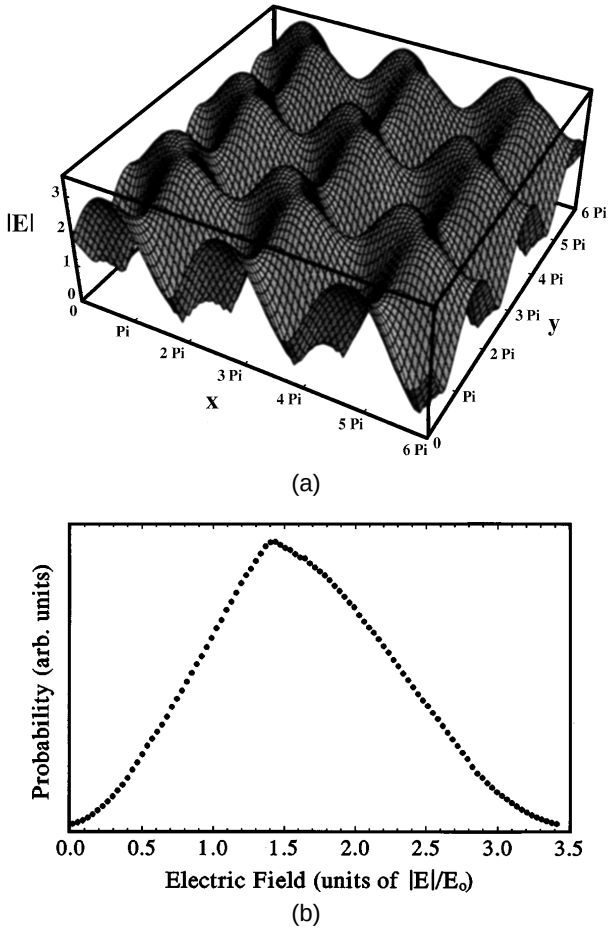

Fig. 6. (a) Local, small-scale structure of the magnitude of the net trapping laser field $|\mathbf{E}_{\text{laser}}|$ for the standard three-dimensional $\sigma^+ - \sigma^-$ MOT configuration. The x and the y axes show the structure over several optical periods for kz fixed at $3\pi/4$. (b) Composite Monte Carlo distribution of the probability of finding a certain $|\mathbf{E}_{\text{laser}}|$ field averaged over random phases in units of $|\mathbf{E}_{\text{laser}}|/E_0$.

dividual line shapes and can be represented by a single effective Rabi frequency.

The important parameters in the numerical model are the decay rates of the cesium levels, the Rabi frequencies for the trapping and the probing laser fields, the detuning of the trapping laser, the magnetic field gradient, and the physical size and shape of the atom cloud. All these parameters are known or measured experimentally. When the atom density is chosen to be proportional to the local field intensity, the model contains no other free parameters except for the signal size, which is used for normalization. For convenient comparisons the height of the larger peak in the model is set equal to the height of the corresponding peak in the experimental data. The Rabi frequency for the probe and the trapping lasers can be calculated from the intensity of the laser beams. At low intensity the probe beam can be considered nonperturbing, although the model is able to calculate the line shape for any value of the probe's Rabi frequency. We control the detuning of the trapping laser experimentally by locking the laser to a saturated absorption signal with a variable-frequency offset. The magnetic-field gradient is calculated from the knowledge of the current and the geometry of the coils. The size of the trap is measured with a CCD camera, which detects the fluorescence of the trapped atoms (in the near infrared at 852 nm). The decay rates of the coupled states are known experimentally, and the decay rates of the uncoupled, artificial states can be estimated by use of simple realistic assumptions. There are many decay paths out of the $9S_{1/2}$ state, and the decay rate depends on which decay path the atom takes. An effective decay rate was estimated with the knowledge of the branching ratios of the possible decay paths. Table 2 shows the range of the values for the important trap parameters, an estimation of the uncertainties, and the qualitative effect of these uncertainties on the line shape.

We turn our attention to the splitting of the levels as a function of various trap parameters. If we first apply a perturbation approach for the probe laser ($\alpha_{32} \approx 0$) and assume a single Rabi frequency across the trap, we can calculate the position of the peaks by solving for the maxima of the imaginary part of σ_{32} {that is, setting $\partial(\mathrm{Im}[\sigma_{32}])/\partial\delta_{32} = 0$ and solving for δ_{32}}. We get an analytic solution for the special case of $\delta_{21} = 0$ (the solution for $\delta_{21} \neq 0$ can be solved numerically). The solution for this case has three values, $\delta_{32} = 0$ and

$$\delta_{32} = \pm\left\{-\frac{\alpha_{21}{}^2}{4}\left(\frac{\gamma_2 + \gamma_3}{\gamma_3}\right) - \frac{1}{16}(\gamma_2 + \gamma_3)^2 + \frac{\alpha_{21}(\gamma_2 + 2\gamma_3)}{8\gamma_3}\left[\alpha_{21}{}^2 + \frac{1}{4}\gamma_3(\gamma_2 + \gamma_3)\right]^{1/2}\right\}^{1/2}. \tag{14}$$

Equation (14) has two values, which represent the Rabi-split peaks; the value $\delta_{32} = 0$ is a local minimum. The splitting and the widths of the peaks depend only on the total lifetimes of the coupled levels, not on the artificial levels for this perturbation approach. This is true for all values of δ_{21}. However, the amplitude of the absorption line shape depends on δ_{21}. This amplitude dependence becomes important when one is considering the whole ensemble of atoms. Therefore the contribution to the total line shape of each Rabi frequency changes as a function of the detuning. At larger detunings the atoms in the larger fields contribute more to the line shape, causing an increase in the effective Rabi frequency compared with those of the line shapes at smaller detunings. This makes it impossible to choose a single value of the electric field to model the splitting dependence on the detuning.

5. COMPARISONS OF THE MODEL AND EXPERIMENT

Our theoretical model works fairly well in reproducing the experimental line shapes. Figure 7 shows a comparison of the theoretical model and the experimental line shape for three different trap detunings δ_{21}. Including the spatial variations of $\mathbf{E}_{\mathrm{laser}}$ and $\mathbf{B}_{\mathrm{trap}}$ and averaging over the phase fluctuations broaden the line shapes as expected and significantly improve the agreement between theory and experiment. For these spectra the best agreement between the model and the experiment occurs with an effective Rabi frequency of ~15.5 MHz. The model reproduces the experimental line shape very accurately at smaller detunings [Fig. 7(a)]. At larger detunings the discrepancies between theory and experiment become more apparent. For most conditions the model predicts a line shape that exhibits the proper linewidths and splittings, but the amplitude of the smaller peak tends to be too small relative to the experimental line shape. The dashed curve in Fig. 7(b) shows the result of the model with a single Rabi frequency under the same conditions as for the solid curve. One can easily see the

Table 2. Important Parameters, Range of Experimental Values, Their Estimated Experimental Uncertainties, and the Qualitative Effect on the Theory[a]

Parameter	Value	Estimated Uncertainty	Relative Effect on Line Shape
Trap diameter (2ρ)	2.5–4.0 mm	±0.3 mm	Small
Trap height ($2z$)	1.3–3.0 mm	±0.3 mm	Small
Magnetic field	$12–20 \times 10^{-4}$ T/cm	$\pm 0.5 \times 10^{-4}$ T/cm	Small
Detuning ($\lvert\delta_{21}/2\pi\rvert$)	4–16 MHz	±0.1 MHz	Very small
Rabi frequency			
α_{21}	12–19 MHz	±1 MHz	Moderate
α_{32}	~0.5 MHz	±0.1 MHz	Small
γ_{nm}	Various	±1–10%	Moderate

[a]The decay rates γ_{nm} are well known for the lower-lying levels, but the uncertainties increase for the higher-lying states.

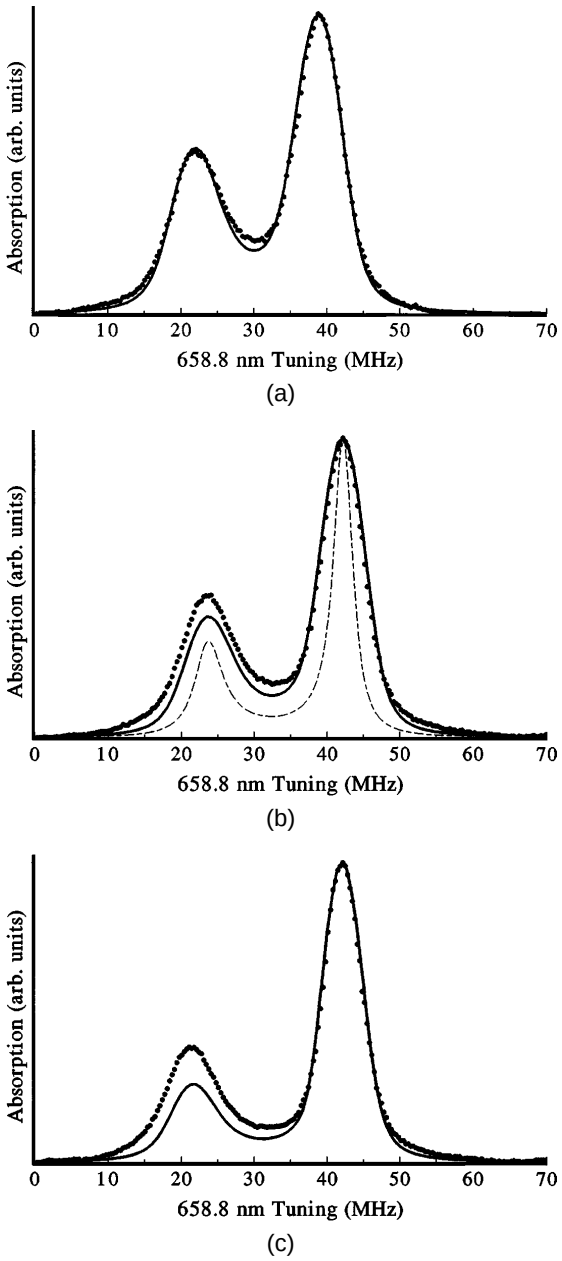

Fig. 7. Experimental and theoretical line shapes with a field gradient of 16×10^{-4} T/cm, an atom cloud diameter of ~3.0 mm, and $\alpha_{\text{effective}} = 15.5$ MHz for various trap laser detunings δ_{21}. (a) $\delta_{21}/2\pi = -7$ MHz, (b) $\delta_{21}/2\pi = -10$ MHz, and (c) $\delta_{21}/2\pi = -13$ MHz. The experimental data are represented by the dots, and the solid curve is the model. The dashed curve in (b) is the theoretical prediction with the same parameters as the solid curve but for a single Rabi frequency.

importance of the electric-field interference pattern and the phase fluctuations by comparing the two predicted line shapes with the experimental data. The electric-field effects broaden the line shape and improve the relative peak height agreement with the experiment. We have chosen model parameters that are realistic for our experiment. (It is possible to change the parameters to unrealistic values to improve the apparent agreement.)

We have investigated the Autler–Townes splitting as a function of the detuning. Inasmuch as the Zeeman shifts of the atomic energy levels increase the complexity of the model, we investigated the splitting both with and without the magnetic-field gradient. The line shapes with the magnetic-field gradient turned off are similar to those shown in Fig. 7, except that the splitting is slightly larger, as expected, because of the larger effective detuning. Figure 8 shows the line-shape splitting as a function of detuning with the magnetic field turned off. The solid curve represents the predicted line-shape splitting. Although the model does a good job of predicting the splitting, a systematic structure at large detunings is not accounted for by the model. It does, however, predict the dependence of the splitting more accurately than if we included only a single Rabi frequency. A study of the splitting with the magnetic field present exhibited similar results, albeit with slightly larger discrepancies between theory and experiment at large detunings. This seems to indicate a need for a more comprehensive treatment of the Zeeman structure.

The two peaks in the Autler–Townes line shape can be interpreted as representing different types of two-photon transition.[12] In the limit where the pump and the probe lasers are very weak ($\alpha_{21} \approx 0$, $\alpha_{32} \approx 0$) and the decay to the artificial levels is negligible (a closed three-level system), the absorption peaks can be interpreted in terms of coherent and incoherent transitions. The smaller peak can be represented by a term that is proportional to σ_{22}, which requires buildup of a population in the $6P_{3/2}$ state. This represents an incoherent two-photon double-resonance peak. The larger, narrow peak can be represented as a term proportional to σ_{21} and corresponds to a two-photon transition with no population in the $6P_{3/2}$ state. To satisfy the conditions for this second type of transition, coherence must be preserved. If the coherence degrades, the transition probability decreases for the coherent peak but increases for the incoherent transition. Therefore, if there are excess relative phase fluctuations, the coherent peak suffers relative to the incoherent peak (the relative height of the smaller peak increases). Most perturbing effects in the laboratory would destroy coherence, thus increasing the apparent relative size of the smaller peak. This effect appears to be small for the laser linewidths (≤ 500 kHz for the trapping laser and ≤ 1 kHz for the probe, as opposed to linewidths of 5.1 MHz for the $6P_{3/2}$ state and ~1 MHz for the $9S_{1/2}$ state) and the collisional effects present in our experi-

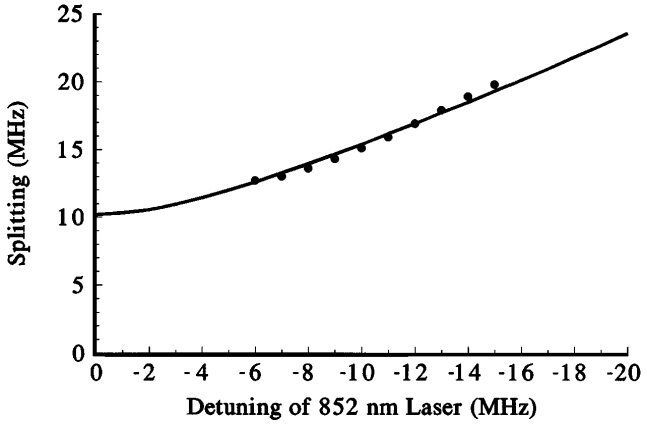

Fig. 8. Splitting of the line shape versus the detuning of the 852-nm laser with the magnetic-field gradient turned off. The solid curve is the numerical result of the model. The error bars on the data are roughly equal to the size of the circles.

ment, and it cannot explain the discrepancies between theory and experiment. Inasmuch as the model and the experiment agree well at small detunings but less so at large detunings, the discrepancy between theory and experiment is in some way dependent on trap conditions. At large detunings we might expect other effects to begin to play a larger role, which would increase the effective Rabi frequency, such as atom localization.

We made a number of simplifications that need to be justified. The first assumption is that the atoms are stationary. In the case of cold trapped cesium atoms the residual Doppler width is small compared with the natural linewidth of the transition (for a sample of cesium atoms cooled to the Doppler limit, the residual Doppler width is ~250 kHz). For Doppler widths in standard cesium traps this effect is small and can be neglected. Similarly, the movement of atoms across the interference pattern of the electric field can be neglected because of the fast cycling frequency and slow atomic velocities. If the intensities of the six laser beams in the trap are not exactly equal or are not uniform across the trapping region (because of the spatial mode variation across the laser beam inherent for diode lasers, for example), the electric field distribution differs from that shown in Fig. 6(b). The peak in the distribution changes position slightly, but the effect on the line shape is surprisingly small. Inasmuch as the Zeeman contribution to the total detuning is small compared with the actual detuning, the effect of other Zeeman levels is expected to be small. Further, as we assume maximum m_F values in the model, inclusion of lower Zeeman coefficients would increase the effective detuning, which tends to degrade the agreement between theory and experiment. To validate further the assumption of large m_F values, a study was done to investigate the polarization of the three-dimensional electric-field distribution. Although for the standard $\sigma^+-\sigma^-$ configuration the electric field is linear everywhere in space for $\phi_n = 0$ [Eq. (11)], changing the relative phases of the laser beams changed the interference pattern. For most choices of the relative phase, the electric field was not linear across the trap but was elliptically polarized. This would tend to optically pump the trapped atoms into the maximum m_F states. This is consistent with our assumption of using only the $m_F = \pm F$ state for each of the coupled states. Other simplifications in the model involved the assumption of plane waves. Because the diameters of the laser beams are large (~1.5 cm) relative to the size of the trap and are well collimated, the approximation of plane waves seems accurate. The inclusion of laser beam geometry would be more important for predictions of other phenomena of trap dynamics that are not confined to the very center of the intersecting beams.

The cascaded two-photon probe also proved useful for studying some of the effects of MOT dynamics. We have used this probe to study some transient properties of the trap following a change in the magnetic field. The trapped atoms took a surprisingly long time to reach equilibrium. We could easily see these properties by monitoring the splitting of the lines as a function of delay after the magnetic field was changed or shut off. The magnetic field in our trap can be switched off in less than 1 ms, yet the splitting of the lines took much longer to reach equilibrium ($\gg 10$ ms). Long time constants in MOT dynamics have also been observed in other laboratories but remain largely unexplained. The slow (order of a few milliseconds) redistribution of atoms between σ^+ and σ^- potential wells has been reported in a four-beam optical lattice and a longitudinal magnetic field.[13] In our six-beam, $\sigma^+-\sigma^-$ MOT there are no true σ^+/σ^- potential wells, but the long time constants may be due to the redistribution of atoms in the trap as the result of other localization or collective effects.

We have also used this system to probe a trap configuration consisting of balls and orbiting rings of atoms that are due to the intentional misalignment of the trapping beams (as seen in other laboratories).[14] This configuration consists of the standard $\sigma^+-\sigma^-$ MOT with two of the pairs of retroreflected laser beams intentionally misaligned in one plane, creating a racetrack composed of

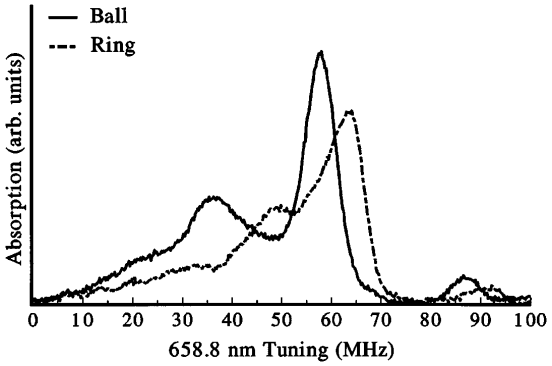

Fig. 9. 658.8-nm absorption spectra of the ring of atoms and the ball of atoms. The MOT parameters were $\delta_{21}/2\pi = -8.5$ MHz and $\partial \mathbf{B}_{\text{trap}}/\partial z = 15 \times 10^{-4}$ T/cm (15 G/cm). The difference between the shapes of the two spectra is due to the large magnetic field at the location of the ring and the electric field amplitude drop-off of the laser beams. The shift in frequency is due primarily to the Doppler shift of the resonant frequency of the moving atoms. The signal size reflects the smaller number of atoms in the ring that intersect the probe laser. The additional features at ~90 and ~25 MHz are sidebands on the probe laser, which are used as a frequency scale. These signals were averaged over 20 scans.

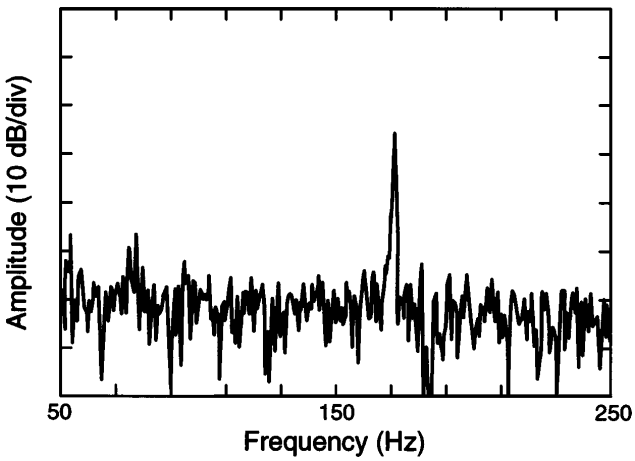

Fig. 10. FFT spectrum of the fluorescence of the MOT showing the narrow frequency component at 170 Hz corresponding to the rotational frequency of the orbiting atoms. The horizontal scale is ~19.5 Hz/division, and the resolution bandwidth is 0.5 Hz. The figure was averaged over 20 scans.

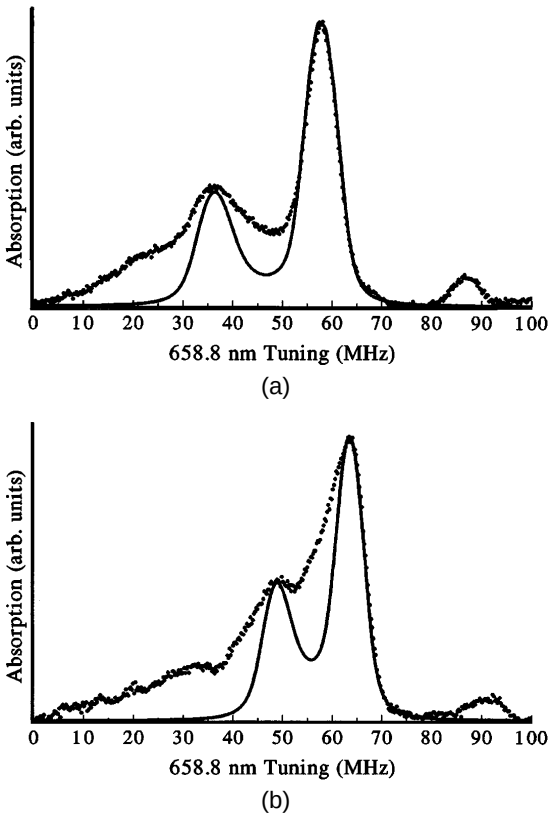

Fig. 11. Comparison of the model and the experiment for the 658.8-nm absorption for (a) the *z* ball and (b) the *z* ring. The data and the trap parameters are the same as in Fig. 9. This model contains no width in the velocity distribution of the orbiting atoms.

four of the laser beams. This configuration shows collective effects of the trapped atoms in which the atoms orbit in stable rings around the center of the trap (which may or may not contain a separate ball of atoms). Our system was aligned to create a ball and ring of atoms in the vertical plane of the experiment. We studied this configuration by observing the differences in the absorption spectra of the 658.8-nm light as it was sent through the ball of atoms versus the ring of atoms. We can compare these two absorption spectra to investigate the environment specific to this particular setup (Fig. 9). Three main properties of the spectra in this figure merit comment. First, owing to the smaller number of trapped atoms in the ball and the ring, the signal-to-noise ratio is much lower than that of previous spectra (the features at ~90 and ~25 MHz are sidebands on the probe laser, which are used as a frequency scale). Second, the Autler–Townes splitting of the line shape of the ball is different from that of the ring. This is expected because of large magnetic fields at the radial position of the rings, as well as the smaller Rabi frequency, which is due to the Gaussian nature of the laser beams (the diameter of the rings was usually ~0.6–1 cm, depending on parameters). Finally, the large frequency shift in the absorption spectra of the orbiting atoms is due mainly to the Doppler shift (there is a small frequency shift from the magnetic fields, as well). With the knowledge of the magnetic-field shift, the smaller Rabi frequency of the laser beams, and the diameter of the orbiting rings, the period of the orbit can be calculated from the Doppler shift. The rotational frequency of atoms in our trap was usually between ~120 and 200 Hz. We used an independent method for determining the rotational frequency of the rings, as well. The bandwidth of the optical detection was fast enough that we could observe the time dependence of the absorption signal as the atoms orbited. This signal was studied in both the time and the frequency domains. A fast Fourier transform (FFT) was used to display the Fourier spectrum of the absorption signal and the signal from the photodetector monitoring trap fluorescence. The FFT spectrum showed a strong and narrow peak at the frequency of the orbiting atoms. Figure 10 shows a typical output of the FFT corresponding to a rotation frequency of 170 Hz. Under most conditions this orbit had a remarkably high Q of several hundred. Figure 11 shows the experimental and modeled line shapes for the two cases of the ring of atoms and the ball of atoms. Our model was able to predict accurately the relative splitting and the relative heights of the line shapes, but the widths of the signal showed poorer agreement.

6. CONCLUSION

We have observed and modeled an Autler–Townes-split optical double-resonance transition for cold atoms in a MOT. The model reproduces the experimental two-photon line shape fairly well under many conditions, particularly for small detunings of the trapping laser and large magnetic-field gradients. It also accurately predicts the splitting of the line shape as a function of the detuning of the trapping laser. The discrepancies between theory and experiment for larger detunings seem to suggest that, although many of the important aspects of the trap, such as the three-dimensional properties of the electric and the magnetic fields, are included in the model, more complexity is needed. We have also used this system as a useful diagnostic for the investigation of collective effects of atoms in a magneto-optic trap. In addition, using the probe laser, we observed transient effects with long time constants that indicate unexplained optical physics in samples of cold trapped atoms.

ACKNOWLEDGMENTS

We acknowledge the helpful comments and discussions of S. Gilbert, R. Fox, and P. Gould and the support of the U.S. Air Force Office of Scientific Research.

REFERENCES AND NOTES

1. K. Gibble and S. Chu, "Future slow-atom frequency standards," Metrologia **29,** 201–212 (1992).
2. See, for example, P. S. Julienne, A. M. Smith, and K. Burnett, "Theory of collisions between laser cooled atoms," Adv. At. Mol. Opt. Phys. **30,** 141–198 (1993).
3. See, for example, feature on laser cooling and trapping of atoms, J. Opt. Soc. Am. B **6**(11) (1989).
4. J. W. R. Tabosa, G. Chen, Z. Hu, R. B. Lee, and H. J. Kimble, "Nonlinear spectroscopy of cold atoms in a spontaneous-force optical trap," Phys. Rev. Lett. **66,** 3245–3248 (1991); G. Grynberg, B. Lounis, P. Verkerk, J.-Y. Courtis, and C. Salomon, "Quantized motion of cold cesium atoms in two- and three-dimensional optical potentials," Phys. Rev. Lett. **70,** 2249–2252 (1993); P. S. Jessen, C. Gerz, P. D. Lett, W. D. Phillips, S. L. Rolston, R. J. C. Spreeuw, and C. I. Westbrook,

"Observation of quantized motion of Rb atoms in an optical field," Phys. Rev. Lett. **69,** 49–52 (1992); A. Hemmerich and T. W. Hänsch, "Two-dimensional atomic crystal bound by light," Phys. Rev. Lett. **70,** 410–413 (1993).
5. P. Marte, R. Dum, R. Taieb, and P. Zoller, "Resonance fluorescence from one-dimensional molasses," Phys. Rev. A **47,** 1378–1390 (1993); J. Guo, "Contribution of energy continuum states to probe absorption signal of atoms in one-dimensional optical molasses," Phys. Rev. A **49,** 3934–3942 (1994); J.-Y. Courtois and G. Grynberg, "Probe transmission in one-dimensional optical molasses: theory for linearly crossed polarized cooling beams," Phys. Rev. A **46,** 7060–7078 (1992).
6. H. R. Gray and C. R. Stroud, Jr., "Autler–Townes effect in double optical resonance," Opt. Commun. **25,** 359–362 (1978); P. R. Hemmer, B. W. Peuse, F. Y. Wu, J. E. Thomas, and S. Ezekiel, "Precision atomic-beam studies of atom-field interactions," Opt. Lett. **6,** 531–533 (1981).
7. R. W. Fox, S. L. Gilbert, L. Hollberg, J. H. Marquardt, and H. G. Robinson, "Optical probing of cold trapped atoms," Opt. Lett. **18,** 1456–1458 (1993).
8. C. Monroe, W. Swann, H. Robinson, and C. Wieman, "Very cold trapped atoms in a vapor cell," Phys. Rev. Lett. **65,** 1571–1574 (1990).
9. V. M. Fain and Ya. I. Khanin, *Quantum Electronics* (MIT Press, Cambridge, Mass., 1969); R. M. Whitley and C. R. Stroud, "Double optical resonance," Phys. Rev. A **14,** 1498–1513 (1976).
10. Initially we assumed that the atom distribution in the atom cloud was random, but we found that the agreement between theory and experiment improved by assuming that the atom density is proportional to the local field intensity. The enhancement of the atom density in the higher fields is expected because of the dipole force that is due to the red-detuned ($\delta_{21} < 0$) laser field.
11. We use cylindrical coordinates. The actual shape of the cloud in our trap is a somewhat irregular, oblate spheroid. The height of the atom cloud (z direction) is approximately two thirds of the diameter and is fairly well represented by a cylindrical volume.
12. S. Stegholm, *Foundations of Laser Spectroscopy* (Wiley, New York, 1984).
13. D. R. Meacher, S. Guibal, C. Mennerat, J.-Y. Courtis, K. I. Pestas, and G. Grynberg, "Paramagnetism in a cesium optical lattice," Phys. Rev. Lett. **74,** 1958–1961 (1995).
14. D. W. Sesko, T. G. Walker, and C. E. Wieman, "Behavior of neutral atoms in a spontaneous force trap," J. Opt. Soc. Am. B **8,** 946–958 (1991); V. S. Bagnato, L. G. Marcassa, M. Oria, G. I. Surdutovich, R. Vitlina, and S. C. Zilio, "Spatial distribution of atoms in a magneto-optical trap," Phys. Rev. A **48,** 3771–3775 (1993).